Stereoscopic Analysis of the 31 August 2007 Prominence Eruption and Coronal Mass Ejection

P.C. Liewer · O. Panasenco · J.R. Hall

Abstract The spectacular prominence eruption and CME of 31 August 2007 are analyzed stereoscopically using data from NASA's twin *Solar Terrestrial Relations Observatory* (STEREO) spacecraft. The technique of tie pointing and triangulation (T&T) is used to reconstruct the prominence (or filament when seen on the disk) before and during the eruption. For the first time, a filament barb is reconstructed in three-dimensions, confirming that the barb connects the filament spine to the solar surface. The chirality of the filament system is determined from the barb and magnetogram and confirmed by the skew of the loops of the post-eruptive arcade relative to the polarity reversal boundary below. The T&T analysis shows that the filament rotates as it erupts in the direction expected for a filament system of the given chirality. While the prominence begins to rotate in the slow-rise phase, most of the rotation occurs during the fast-rise phase, after formation of the CME begins. The stereoscopic analysis also allows us to analyze the spatial relationships among various features of the eruption including the pre-eruptive filament, the flare ribbons, the erupting prominence, and the cavity of the coronal mass ejection (CME). We find that erupting prominence strands and the CME have different (non-radial) trajectories; we relate the trajectories to the structure of the coronal magnetic fields. The possible cause of the eruption is also discussed.

Keywords Corona · Coronal mass ejection · Filament eruption · Prominence

P.C. Liewer (✉) · J.R. Hall
Jet Propulsion Laboratory, California Institute of Technology, Pasadena, CA 91109, USA
e-mail: Paulett.Liewer@jpl.nasa.gov

O. Panasenco
Helio Research, La Crescenta, CA 91214, USA

1. Introduction

The study of prominence eruptions is receiving increased attention because of their close association with coronal mass ejections (CMEs; Gopalswamy *et al.*, 2003). It is now recognized that the filament (called prominence when at the limb), the filament channel encompassing the polarity reversal boundary, the overlying arcade and the CME itself are all part of one linked magnetic system (Martin *et al.*, 2008; Pevtsov, Panasenco, and Martin, 2012). The filament eruption does not cause the CME nor visa versa; rather, they are two manifestations of the same underlying magnetic phenomenon. Thus, by studying filament eruptions, we can better understand the cause of CMEs and improve our ability to predict these space-weather drivers. A CME may occur at the site of an empty filament channel (Pevtsov, Panasenco, and Martin, 2012), but when the filament is visible, it can provide important information on the chirality and helicity of the magnetic system, as well as its evolution, prior to CME initiation.

The launch of the twin *Solar Terrestrial Relations Observatory* (STEREO) spacecraft in October 2006 has provided the opportunity to view filament and CME eruptions from two viewpoints, giving new insights into the three-dimensional geometry and the relationships between various features associated with these eruptions. Each spacecraft of the STEREO mission carries four remote sensing and *in situ* instrument suites (Kaiser, 2005). The *Sun Earth Connection Coronal and Heliospheric Investigation* (SECCHI) imaging package on each spacecraft includes five telescopes: an *Extreme Ultra Violet Imager* (EUVI), inner (COR1) and outer (COR2) coronagraphs, and inner (HI1) and outer (HI2) heliospheric imagers (Howard *et al.*, 2008). The EUVI telescope has four channels similar to those of the *Extreme ultraviolet Imaging Telescope* (EIT) on the *Solar and Heliospheric Observatory* (SOHO). The wavelengths and coronal temperature of peak response are 304 Å ($6 - 8 \times 10^4$ K, primarily the He II line), 171 Å (10^6 K, primarily Fe IX/X), 195 Å (1.4×10^6 K, primarily the Fe XII line) and 284 Å (2.2×10^6 K) (Wuelser *et al.*, 2004). The standard SECCHI synoptic program running during the eruption provided simultaneous A – B pairs at a ten min cadence for 304 Å and 195 Å and a 2.5 min cadence for 171 Å. SECCHI data are available through the STEREO Science Center (http://stereo-ssc.nascom.nasa.gov).

Since the launch of STEREO, there have been several studies of prominences that use the two viewpoints to reveal new features of prominences and filaments and their relationship to solar processes (Liewer *et al.*, 2009; Gosain *et al.*, 2009; Bemporad, 2009; Li *et al.*, 2010; Xu, Jing, and Wang, 2010; Li *et al.*, 2010, 2011; Thompson, 2011; Bemporad, Mierla, and Tripathi, 2011; Panasenco *et al.*, 2011). In several of these, the stereoscopic images from the twin spacecraft were used to reconstruct prominence in three-dimensions (3D) before and/or during the eruption to study various aspects of the eruption trajectory such as the true time-height plot (Liewer *et al.*, 2009; Bemporad, 2009; Li *et al.*, 2010, 2011) and the amount of rotation (Thompson, 2011; Bemporad, Mierla, and Tripathi, 2011).

Here, we use the stereoscopic technique of tie-point and triangulation to analyze the prominence eruption and CME of 31 August 2007 using data from the twin STEREO spacecraft. The filament was stable for its entire passage across the solar disk until it erupted spectacularly as it reached the east limb. We were able to reconstruct in 3D the filament before and during the eruption using images in both extreme ultraviolet and white light (SECCHI EUVI and COR1). Prior to the eruption, we were able to reconstruct in 3D, for the first time, a barb on the filament connecting the spine to the solar surface. The prominence rotates clockwise through about 90° as it erupts. The rotation is in the direction expected for a filament system of the observed chirality (determined from the barb and the magnetogram and confirmed by other signatures as discussed below). As the filament erupts, the endpoints

where it connects to the surface are observed to change; fan-like EUV brightenings, as discussed by Wang, Muglach, and Kliem (2009), are seen at the location of the new endpoints, which are also sites of strong downflows. These appear near the beginning of the fast-rise phase of the eruption as the CME begins to form. The 3D reconstructions allow us to study the spatial relationships among various features of the eruption including the pre-eruptive prominence, flare ribbons, the erupting prominence, the EUV brightenings and the CME cavity. We are also able to compare non-radial trajectories of erupting filament strands and the CME and relate these to the coronal magnetic fields as computed from a Potential Field Source Surface model.

This paper is organized as follows. In Section 2, the stereoscopic analysis technique used to analyze the eruption is described. Section 3 presents the results of the analysis of the pre-eruptive prominence and the determination of the chirality of the system. Section 4 presents the results of the analysis of the prominence eruption, rotation, rolling and trajectory, and the relation to observed EUV brightenings and appearance of flare ribbons. Section 5 presents results from stereoscopic analysis of the spatial relationship between the prominence and CME during the eruption and relates these to the structure of the coronal magnetic fields. The possible cause of the eruption is also discussed. Section 6 contains a summary and discussion.

2. Stereoscopic Analysis Technique

In this paper, we use the technique of tie-pointing and triangulation (T&T) to perform a stereoscopic analysis of the spectacular prominence and CME eruptions of 31 August 2007 using data from the SECCHI instruments on the twin STEREO spacecraft. Two movies of these eruptions from STEREO B, one from EUVI 304 Å and one from COR1, are included in the electronic supplementary material. The T&T technique as applied to data from STEREO is described in Aschwanden *et al.* (2008) and Liewer *et al.* (2009). The software tool we use, SUNLOOP, described in Liewer *et al.* (2009), is available in the SolarSoft library. Briefly, the tool is first used to locate and mark the same features in both images of a simultaneous pair, one from each of the STEREO spacecraft. The tie-points are constrained to lie in an epipolar line as discussed in Liewer *et al.* (2009) and Inhester (2006). A sample stereoscopic pair with the tie-points is shown in Figure 1, which shows the erupting prominence at 31 August 2007 at 20:42:15 UT as imaged in 304 Å by the EUVI telescopes; the STEREO-B (A) image is on the left (right). Triangulation is then used to determine the 3D location in a heliographic coordinate system of each of the tie-pointed features; the points are connected with straight-line segments to reconstruct the prominence in 3D. The tool also allows the user to rotate and view the 3D reconstruction from any vantage point (see Figure 2).

Figure 2 shows the 3D reconstruction of the erupting filament loop from the tie-points in Figure 1 (green loop) as seen from two vantage points: approximately along the direction of the eruption (left) and edge-on (right). Also shown are the 3D reconstructions of the pre-eruption U-shaped filament (orange) on 23 August 2007 (reconstructed from a 304 Å stereoscopic pair on 23 August at 01:46:14 UT) and the post-eruption flare ribbons (reconstructed from a 304 Å pair on 31 August at 20:58:45 UT). This illustrates that by using this stereoscopic analysis technique, we can determine the spatial relations between the various features of this prominence eruption. For example, Figure 2 shows that the endpoints of the erupting prominence at 31 August 2007 10:21:15 UT (green loop) are located at some distance from the pre-eruptive filament (orange loop) and the flare ribbons (blue segments).
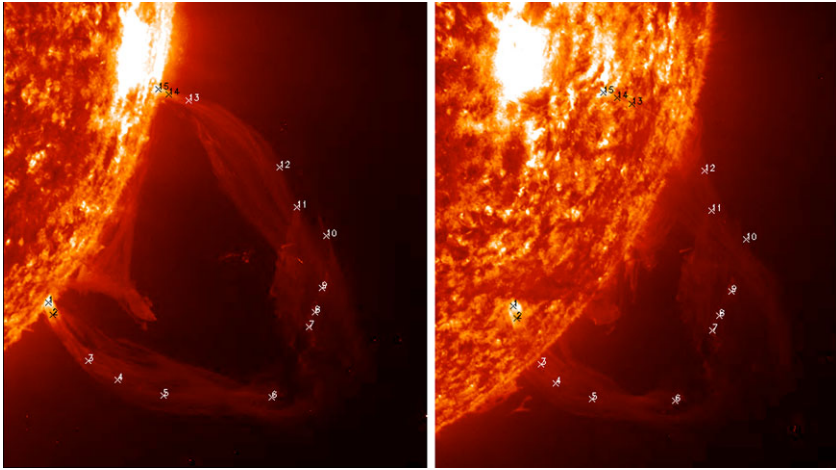
Figure 1 Sample of a stereoscopic pair used to analyze the eruption. Here, the erupting prominence with tie-points is shown at 31 August 2007 20:42:15 UT 2007. The 304 Å STEREO-B (A) image is on the left (right).
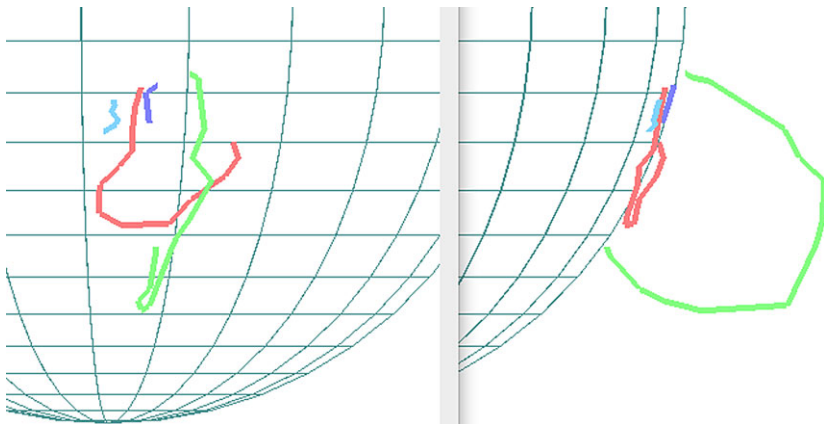

Figure 2 Two views of the 3D reconstruction of the erupting prominence from the tie-points in Figure 1 (green loop). Also shown are 3D reconstructions of the pre-eruption U-shaped filament (orange) on 23 August 2007 and the post-eruption flare ribbons at 20:58:45 UT on 31 August.

This spatial relationship as well as others, such as the spatial relationship between the erupting prominences and the CME cavity, will be discussed in the sections to follow.

3. Stereoscopic Analysis of Pre-eruptive Filament

3.1. Solar Context for the Eruption

A filament with a U-shaped filament channel was seen at east limb on 22 August 2007 in 304 Å by both STEREO spacecraft; it retained this U shape during the entire disk passage until its eruption on 31 August 2007 as it reached the west limb. Figure 3 shows the corona (top panel: 195 Å image) and the U-shaped filament (middle panel: 304 Å image) on 25
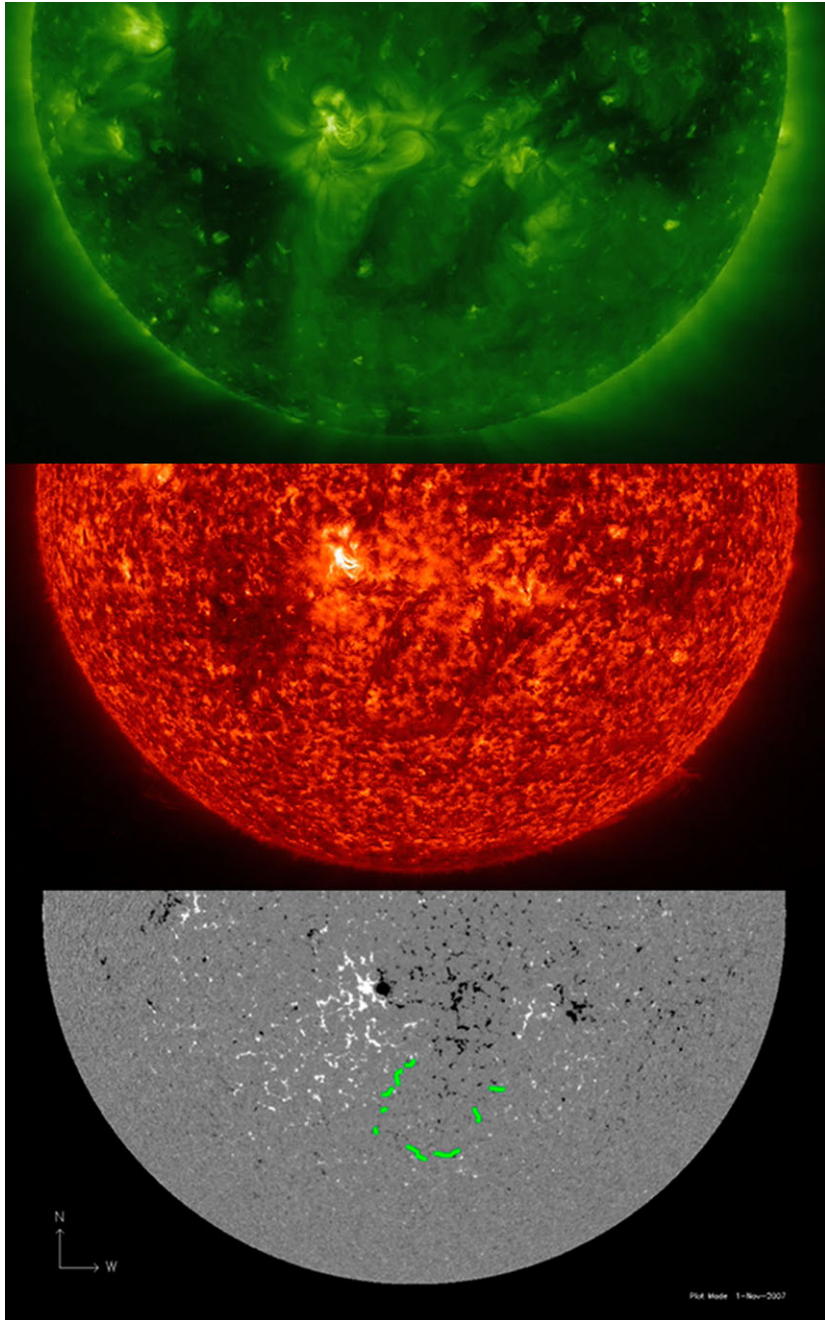
Figure 3 Filament context on 27 August 2007. Top: EUVI B 195 Å image showing dark U-shaped coronal filament cavity (channel) at 23:55:30 UT. Middle: EUVI B 304 Å image at 23:56:15 UT showing the U-shaped filament spine. Bottom: SOHO/MDI magnetogram at 04:51 UT with an overlay of the filament as seen in Hα at 06:01 UT.

August 2007 as seen by STEREO-B. The bottom panel of Figure 3 shows the *Solar and Heliospheric Observatory* (SOHO) *Michelson Doppler Imager* (MDI) magnetogram for the region on 27 August 2007 with an overlay (in green) of the filament as seen in Hα on the same day (Kanzelhoehe Solar Observatory, 06:01:07 UT). The upper panel of the corona (23:55:30 UT) shows a dark cavity region surrounding the U-shaped filament, whose spine is clearly visible in the middle panel (23:56:15 UT). Filament cavities are regions of lower density plasma (Gibson *et al.*, 2010). The filament is a tracer of the strongly sheared non-potential magnetic field structure confined by the overlying coronal magnetic fields.

A large coronal hole can be seen to the east of the filament channel in the 195 Å image (top panel of Figure 3). Near the top of the left side of the U is a new active region AR 10969; near the top of the right side of the U is an older decaying active region. There is considerable magnetic evolution occurring in the magnetic fields surrounding the filament throughout its disk passage, including eruptions in the decaying active region on 23 August (with a visible prominence eruption) and 24 August that left the U-shaped filament generally unaffected. From the bottom panel, it can be seen that the U-shaped filament spine lies above the polarity reversal zone separating regions of predominantly positive (white – outside the U) and predominantly negative (black – inside the U) photospheric magnetic fields. This information is needed to determine the chirality of the filament system. The new active region to the NE and the old decaying active region to the NW are also evident in this magnetogram.

3.2. Reconstruction of Pre-eruptive Prominence: Barb and Chirality

Filaments lie above photospheric polarity reversal boundaries separating regions of predominantly opposite magnetic polarity. They often show lateral extensions, called barbs, which are associated with small regions of minority polarity on each side of the filament (Martin, 1998, 2003; Martin, Lin, and Engvold, 2008). Here, for the first time, we are able to reconstruct a barb in 3D, confirming that the barb connects the filament spine to the surface. The left panel of Figure 4 shows an image of the filament on 26 August at 00:06:15 UT in 304 Å as seen from STEREO-A; a left-bearing barb can be seen on the inner side of the U-shaped spine (indicated by arrow). We were able to trace and "tie-point" the barb from near the surface up to the filament spine. The middle panel of Figure 4 shows the 3D reconstruction of the filament spine (east U-segment – orange; west U-segment – blue) and barb (short green segment) from a similar viewpoint as STEREO-A; on the right is a side view showing the barb going from the surface ($R = 1.00\ R_{\text{sun}}$) up to the filament spine at $1.02\ R_{\text{sun}}$.

Barbs are important because, given the magnetogram and a barb orientation relative to the filament spine, the chirality, handedness, and helicity of a filament system, the skew of the overlying magnetic arcade and the minority polarity associated with the barb can be determined. A left-bearing barb, as seen here, implies a positive polarity (minor polarity) at its base, a sinistral filament that has a "right-skewed" overlying arcade; the filament-arcade system is right handed with positive helicity (Martin, 1998, 2003; Martin, Lin, and Engvold, 2008). For the eastern segment of the U-shaped spine, since the magnetic field is positive outside the U, the magnetic field of the filament is directed northward along this segment (indicated by the black arrow on the middle panel), and the overlying arcade should be skewed somewhat clockwise relative the filament spine (Martin, 2003). This implies that during the eruption, the filament should rotate clockwise to bring the magnetic field lines of the filament more in alignment with the overlying arcade, reducing the magnetic stress.
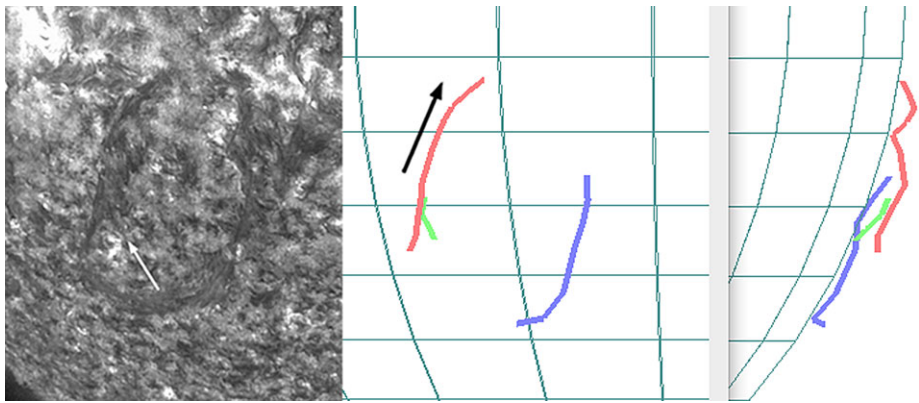
Figure 4 Left: Filament showing a left-bearing barb (arrow); the STEREO-A 304 Å image is from 26 August at 00:06:15 UT. Center and right: 3D reconstructions of the spine (east U-segment – orange; west U-segment – blue) and the barb (short green segment) from two viewpoints: similar to STEREO-A (center) and edge on (right). The black arrow indicates the direction of the filament magnetic field.

Figure 5 Cartoon showing the magnetic topology of the filament system expected for a sinistral filament with positive helicity (right handed) and photospheric polarities as shown. Green lines – filament magnetic field lines with barb associated with minor polarity; black lines – magnetic field lines of cavity; blue lines – overlying skewed arcade magnetic field lines. See text.
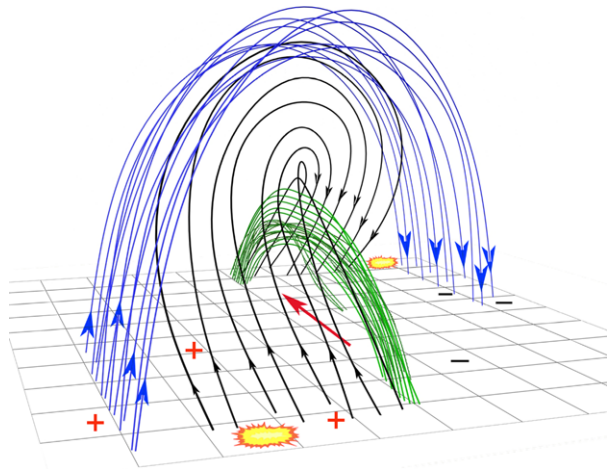
A cartoon of the expected filament magnetic field structure and the overlying arcade for a sinistral filament, such as the eastern segment of the U-filament, is shown in Figure 5. The blue field lines represent the right-skewed arcade field overlying the filament. For our U-shaped filament, the field lines cross from the outside to the inside of the eastern segment of the U. The black lines represent the sheared filament cavity field lines and the green represent the filament field lines, including a left-bearing barb. The filament lies above the polarity reversal boundary. The yellow spots are in the approximate locations of EUV brightenings expected for a such a right-handed filament system (Wang, Muglach, and Kliem, 2009), discussed in Section 4.2.
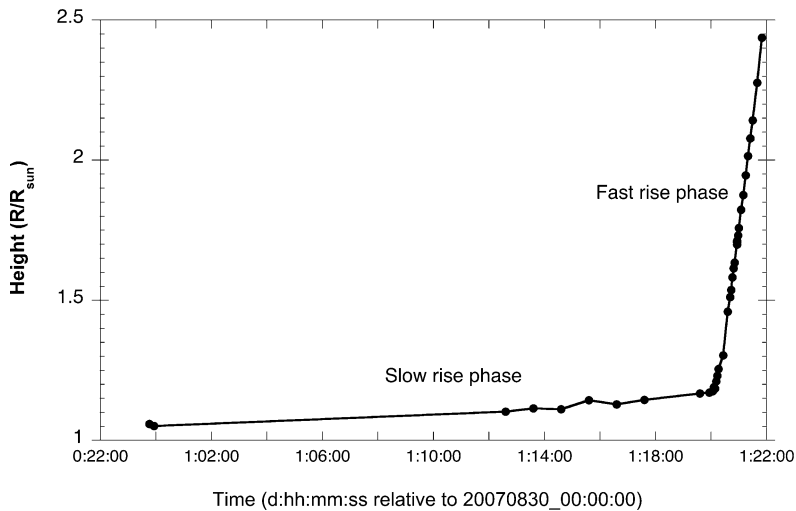
Figure 6 True height-time plot for the filament eruption from 3D reconstructions using both EUVI and COR1 stereoscopic pairs showing a transition from slow to fast rise occurring just after 1:20:20 (20:20 UT on 31 August). Flare ribbons begin to appear at approximately 1:20:40 UT (20:40 UT on 31 August).

4. Stereoscopic Analysis of Erupting Prominence Trajectory and Rotation

4.1. Prominence Trajectory and Rotation

The filament could be analyzed stereoscopically for many days before and during the eruption using both the EUVI 304 Å images and the COR1 white light images. Two 3D filament reconstructions have been shown in Figures 2 and 4. The eruption could be followed seamlessly from the EUVI to the COR1 fields of view. At the times when the filament was visible to both spacecraft in both instrument's fields of view, the 3D reconstructions from the EUVI and COR1 stereo pairs coincided exactly, as they should if the spacecraft pointing information and our stereoscopy tools are working correctly.

From the 3D reconstructions, we have constructed the "true" (3D) height–time plot, shown in Figure 6 for the last day only, including information from T&T reconstructions from both EUVI and COR1. The height is taken as the highest point on the reconstruction at each time, not by following a single feature. The pre-eruptive maximum height was about 1.05 R_{sun}; this was the height throughout disk passage from our first reconstruction on 23 August 2007 at 01:46:15 UT until late on 30 August when a slow rise phase began. The plot in Figure 6 begins at 30 August 2007 23:46:15 UT, near the start of the slow rise phase. From the plot, we can clearly identify the transition between the slow and fast rise phases for this eruption which occurs just after 20:00 UT on 31 August (Time = 1:20:20 in Figure 6). Figure 1 showed the eruption at 20:41:15 UT; at this time (about 40 min into the fast rise phase) the height was $R = 1.5 \ R_{sun}$. Also at this time ($\approx$ 20:40 UT) the flare ribbons begin to appear; we interpret this as the time when the magnetic structure of the CME begins to disconnect from the Sun. The relation to the CME eruption is discussed further in Section 5.

Figure 7 shows the T&T reconstructions of the top of the primary filament segment at several times during the eruption on 31 August 2007. Here, and in other figures showing 3D reconstructions, the straight green line emanating from the origin of the coordinate system indicates the direction to Earth and the straight blue (red) line indicates the

Figure 7 3D reconstructions of the prominence eruption using stereoscopic pairs from EUVI and COR1 from 16:36:15 to 20:58:45 UT on 31 August 2007. The transition from slow to fast rise occurs at ≈ 20:00 UT; flare ribbons begin to appear at ≈ 20:41 UT (14 min after the very short blue segment from 20:26:15 UT) and are well developed by 20:58:45 UT (see reconstruction in Figure 2).
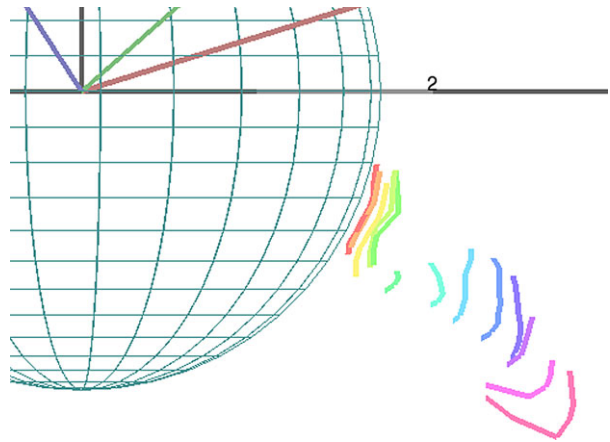

direction to STEREO-B (A). The first ten reconstructions are from EUVI 304 Å stereoscopic pairs at the times 16:36:15 UT (1.13 R_{sun}), 17:36:15 UT (1.14 R_{sun}), 19:36:15 UT (1.17 R_{sun}), 20:08:45 UT (1.18 R_{sun}), 20:11:15 UT (1.21 R_{sun}), 20:26:15 UT (short blue segment, 1.30 R_{sun}), 20:36:15 UT (1.46 R_{sun}), 20:43:45 (1.54 R_{sun}), 20:51:15 (1.63 R_{sun}), and 20:58:45 UT (1.73 R_{sun}); the last three reconstructions are from COR1 stereoscopic pairs at 21:00 UT (1.76 R_{sun}), 21:10 UT (1.88 R_{sun}) and 21:20 UT (2.01 R_{sun}). Again, we are not always able to identify the same features in each stereoscopic pair and the height given is the maximum radius for that reconstructed segment. The transition from slow to fast rise phase on 31 August at ≈ 20:00 UT is at the time of the fourth reconstruction (green at 20:11:15 UT with $R = 1.21\ R_{sun}$ – segment before the very short blue segment). The segment following the short blue segment (20:36:15 UT $-1.46\ R_{sun}$) is from approximately the time flare ribbons first appear. The reconstruction of the filament at 20:58:45 UT is from the same time as the reconstruction of the more developed flare ribbons shown in Figure 2.

Figure 8 shows the same reconstructions shown in Figure 7, but now re-projected down to the surface ($R = R_{sun}$). In this way, the rotation of the filament can be seen without the confusion caused by projection effects. The rotation of this filament has also been determined using stereoscopy by Bemporad, Mierla, and Tripathi (2011). Note the clockwise rotation of the filament through about 90°. This is the direction of rotation expected from the sinistral chirality of this prominence (see Wang, Muglach, and Kliem (2009) and references therein). As it rises, it becomes more aligned with the overlying arcade field in response to the magnetic stresses. Inspection of Figures 7 and 8 show that the rotation begins during the slow rise phase (to ≈ 20:00 UT, 6 min prior to the time of very short blue segment from 20:26:15 UT), but most of the rotation occurs during the fast rise phase. The projections in Figure 8 also show that this prominence segment does not move out radially, but rather follows a curved trajectory southward and westward.

If a filament erupts non-radially, as in this case and many others, the top of its spine first bends to one side and the filament develops a sideways rolling motion called the *roll effect* (Martin, 2003; Panasenco and Martin, 2008; Panasenco *et al.*, 2011, 2012). These four studies found that the roll effect appears during the beginning phase of the prominence eruption, before CME formation begins; it is caused by asymmetries in the arcade overlying the filament. These studies also showed that the overlying arcade, filament cavity, filament and CME rise together during the CME eruptions, but the roll effect occurs earlier and shows itself as a smaller scale motion, lower down in the corona. Any non-radial effects on

Figure 8 The same 3D reconstruction as in Figure 7, but re-projected down to the surface ($R = R_{sun}$). Note the clockwise rotation of the filament through about 90°. See text and caption for Figure 7.
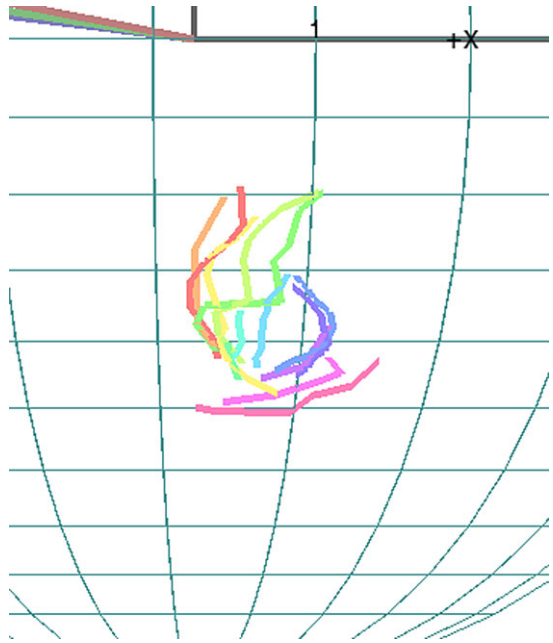
the larger scale eruption of the whole filament system and CME are caused by the larger scale magnetic structure of the corona (Panasenco *et al.*, 2011, 2012; Pevtsov, Panasenco, and Martin, 2012).

From Figure 8 it can be seen that, in this case as well, the sideways rolling motion of the prominence is very strong for the first seven reconstructions in Figures 7 and 8. Inspection of the reconstructions show a lateral rolling motion of the prominence of about 8° in latitude as it rises to 1.46 R_{sun} (20:36 UT). After this time, the motion becomes more rotational and less lateral (last six reconstructions in Figures 7 and 8). This change is due to the influence of the overlying filament channel magnetic field, which has a right-handed skew similar to the arcade and forces the sinistral filament to rotate clock-wise during its eruption. The relation between the prominence and CME non-radial motions and the relation to the coronal magnetic fields are discussed further in Section 5.

4.2. Formation of New Filament Endpoints and EUV Brightenings

Only the east leg of the U-shaped filament erupted; the western segment was still visible as it rotated over the west limb. Both the observations and reconstructions show that as the filament erupts and rotates, the locations of the endpoints of the erupting portion of the filament change. Figure 1 showed the filament at 20:41:15 UT as seen by STEREO-B, part way into the fast rise phase ($R_{max} = 1.5 R_{sun}$). The tie-points follow the main filament segment at this time and show endpoints in a different location than earlier in the eruption; one of the original pre-eruption filament endpoints can be seen in Figure 1 as the tower-like object sticking up below the erupting filament. Figure 9 shows the filament earlier (31 August 19:56:15 UT, near the end of the slow rise phase) when it is still connected to the surface through this tower; the view from STEREO-B (A) is on the left (right). The new endpoint forming is also visible in the view from STEREO-B (also see movie 20070831_EUVI_B_304.mov (Electronic Supplementary Material) 20:00 to 20:50 UT).
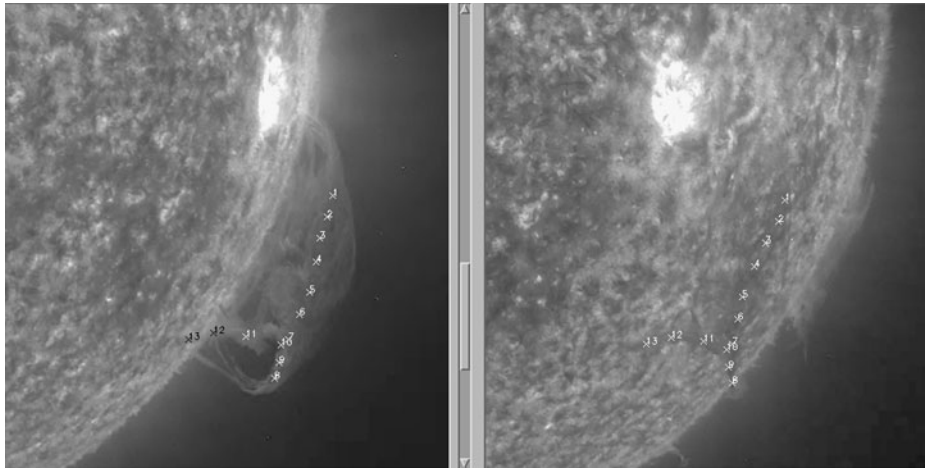
Figure 9 EUV 304 Å image pair with tie-points for 31 August at 19:56:15 UT showing the filament connected to the surface through the tower-like structure seen in Figure 1. The 304 Å STEREO-B (A) image is on the left (right).
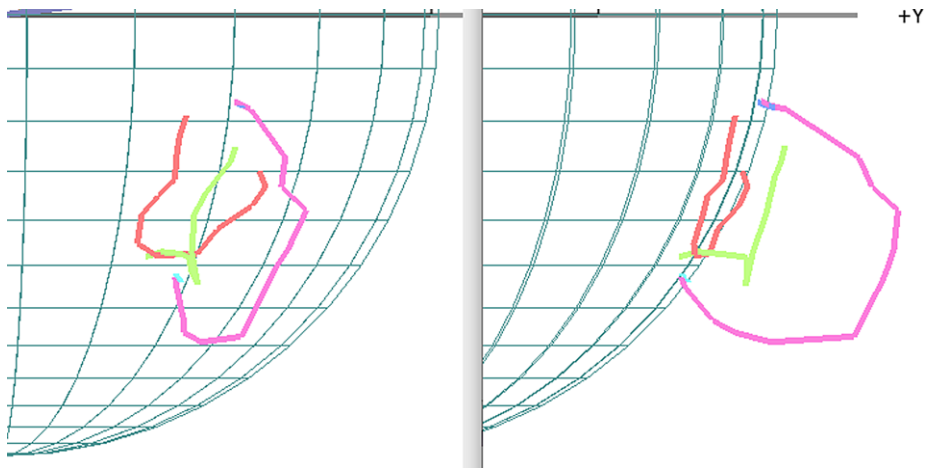

Figure 10 3D reconstructions of the filament at three times: The pale green segment is the reconstruction of the filament from the tie-points in Figure 9 (31 August at 19:56:15 UT); the quiet filament from 23 August (orange); and the erupting filament on 31 August at 20:41:14 (magenta – also seen in Figures 1 and 2). Also shown are the locations of the EUV brightenings on 31 August at 20:41:00 UT, determined stereoscopically (very small blue segments).

Figure 10 shows the 3D reconstruction of the filament at 19:56:15 UT (pale green) from the tie-points in Figure 9; also shown for context are the reconstructions of the quiet filament from 23 August (orange) and the erupting filament 31 August 20:41:14 UT (large magenta loop – also seen in Figures 1 and 2). The filament at 19:56:15 UT (pale green) is connected to the surface at a location that coincides with the pre-eruptive filament (orange). The subsequent reconstruction at 20:41:14 UT (the approximate time flare ribbons first appear) shows that the location of the filament's endpoints have changed. From Figure 10 it can be seen that
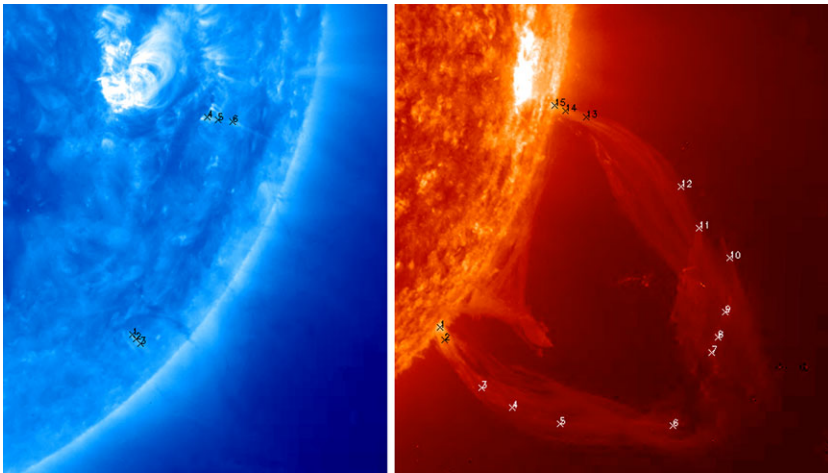
Figure 11 Left: STEREO-A 171 Å image on 31 August at 20:41:00 UT with tie-points on the EUV bright-enings. On the right is the nearly simultaneous STEREO-B 304 Å image (at 20:41:15 UT) showing bright filament footpoints that are also sites of strong downflows.

the new endpoints of the erupting filament at 20:41:14 UT (magenta) are at some distance from the pre-eruption filament (orange) and thus from the center of the filament channel.

Barely visible in Figure 10 are the reconstructions of two EUV brightenings observed at 20:41:00 UT (very short blue segments). The 3D locations of the EUV brightenings were obtained from T&T using a 171 Å stereoscopic pair on 31 August at 20:41:00 UT. The fan-shaped brightenings appear at about the same time as the flare ribbons' first appear. The STEREO-A 171 Å image at this time is on the left in Figure 11 with the tie-points placed on the brightenings. On the right is the nearly simultaneous STEREO-B 304 Å image (at 20:41:15 UT). From the T&T analysis of both the 171 and 304 Å stereoscopic pairs at 20:41:00 and 20:41:15 UT respectively, we have verified that the EUV brightenings are co-located with the new bright filament endpoints seen in the STEREO-B 304 Å image. Figure 10 also shows that the reconstruction of these brightenings (very short blue segments) coincide with the end points of the loop from 20:41:14 UT (magenta).

The observations that i) the EUV brightenings and new endpoints are co-located and ii) that they appear at some distance from the center of the filament channel are consistent with the analysis of such brightenings by Wang, Muglach, and Kliem (2009). In that paper, they find that the spike-like or fan-shaped brightenings occur at the outer boundaries of the filament channel and that they are most intense at the time of maximum CME acceleration. They interpret the brightenings as the footpoints of the current sheets formed at the leading edge of the erupting filament magnetic fields as these fields reconnect with the overlying arcade. Our analysis supports this interpretation. The brightenings appear near the start of the fast rise phase, which is the time during which the filament (still rotating) and newly formed CME are pushing out through, and presumably reconnecting with, the overlying coronal fields. Strong downflows are observed in these new filament endpoints (see movie 20070831_EUVI_B_304.mov in the Electronic Supplementary Material at 21:00 UT), possibly causing the brightenings, consistent with interpretation as the footpoints of the current sheets. Wang, Muglach, and Kliem (2009) also find that the brightening lie near the outer edges of the transient coronal hole created by the CME; unfortunately, any transient coronal holes were not visible for this CME because its location at the west limb. We speculate that

Figure 12 Right-skewed post-eruptive arcade as seen in the STEREO-A 195 Å image at 21:55:30 UT from STEREO-A. This confirms the chirality inferred from the barb and magnetogram.
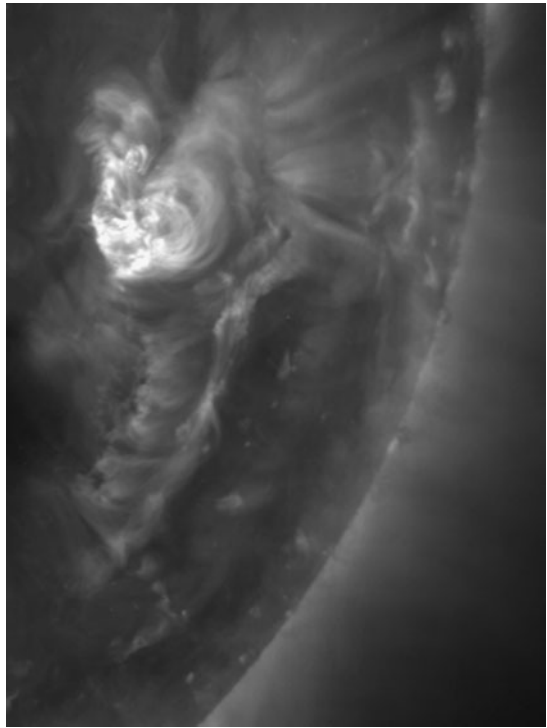
these new endpoints are related to the "spurs" identified in Thompson (2011), which were also related to sites of strong downflows.

Wang, Muglach, and Kliem (2009) showed that the location of the brightenings relative to the filament channel can be used to determine unambiguously the direction of the filament magnetic field. Here, we use the location of the brightening to confirm the field direction determined by us using the barb and the magnetogram (sinistral filament with right-skewed arcade). In Figure 10, it can be seen that the upper brightening and new filament endpoint are located to the west of the polarity reversal boundary as delineated by the 23 August filament reconstruction (orange) and the lower brightening and filament endpoint is to the south. These indeed are the general locations predicted by Wang, Muglach, and Kliem (2009) for a sinister filament with a right-skewed arcade. The fact that the overlying arcade is right-skewed is further confirmed in Figure 12, which shows the right-skewed post-eruptive arcade as seen in the 195 Å image at 21:55:30 UT from STEREO A. Thus the topology of the system of the cartoon in Figure 5 is confirmed; the yellow spots in Figure 5 show the expected locations of the brightenings.

5. Stereoscopic Analysis of the CME and Relation to Prominence

The CME associated with this filament eruption was analyzed stereoscopically to determine the spatial relationship between the erupting filament and the CME and to determine the CME trajectory using the technique described in Liewer *et al.* (2011). The erupting east leg of the U-shaped spine was observed to break into several segments as it erupted. Figure 13 shows a stereoscopic pairs from SECCHI COR1 on 31 August at 21:20:00 UT showing
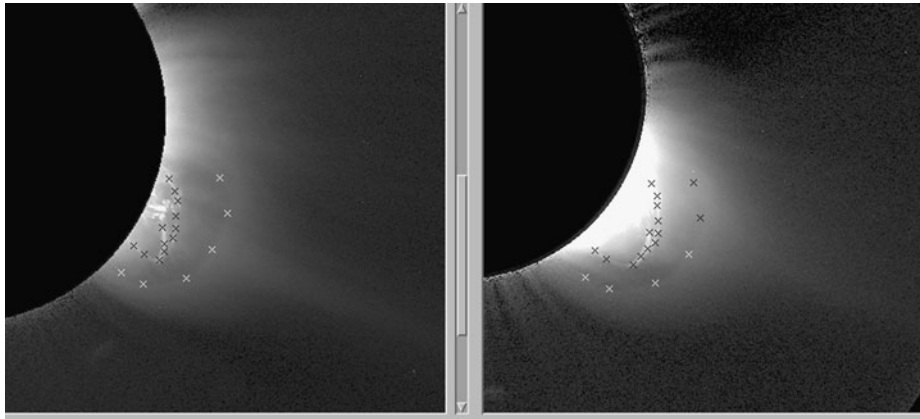
Figure 13 SECCHI COR1 stereoscopic pairs on 31 August at 21:20:00 with tie points on two segments of the erupting prominence and the inner edge of the CME cavity. The STEREO-B (A) image is on the left (right). The reconstructions from these tie-points are shown in Figure 14.
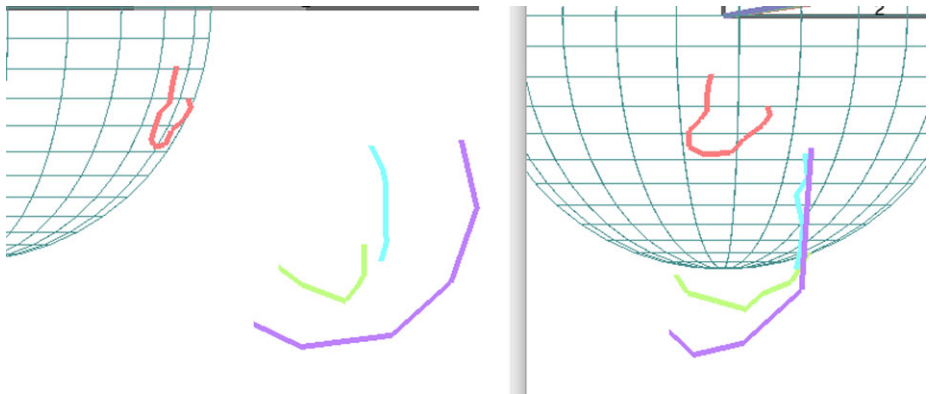

Figure 14 Two views of the 3D reconstructions of the primary (green) and secondary (blue) filament segments and the inner edge of the CME cavity (purple) from the tie-points in Figure 13, at 31 August 2007 21:20:00 UT. For reference, the reconstruction of the quiet pre-eruption filament from 23 August is also shown (orange).

tie points on two segments of the erupting prominence and the inner edge of the CME cavity (see also movie 20070831_COR1_B.mov in the Electronic Supplementary Material). We note that both filament segments can be accurately reconstructed in 3D because the white light emission is from a structure that is well localized spatially. However, CMEs are extended optically thin features scattering white light; what appears as the bright cavity edge is a line-of-sight effect as discussed by Meirla *et al.* (2010) and Liewer *et al.* (2011). For the small spacecraft separation in August 2007 ($\approx 28°$), the reconstruction from these tie-points should be a good approximation to the leading edge of the cavity, but the 3D shape cannot be determined.

The 3D reconstructions of the primary (pale green) and secondary (blue) erupting filament segments and the inner edge of the cavity from the tie-points are shown in Figure 14. The reconstruction of the primary segment was also shown in Figure 7 (furthest out – pink
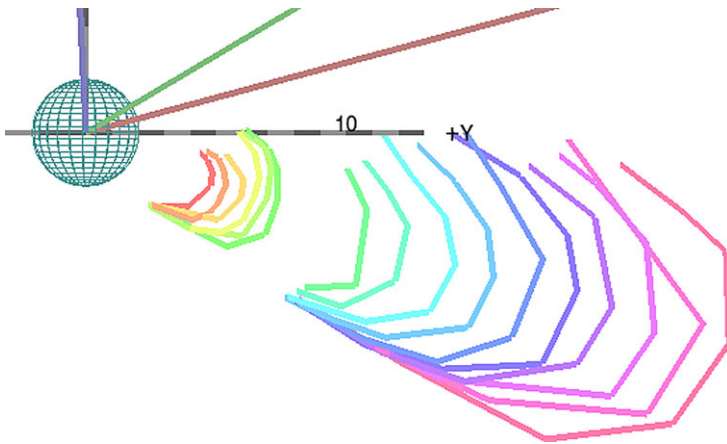
Figure 15 Reconstructions of the leading edge of the CME using stereoscopic pairs from both COR1 (first six reconstructions) and COR2 (last ten reconstructions).

segment) and, projected onto the solar disk, in Figure 8. Both filament segments appear to be within the CME. This is the case, even is cases where the filament and CME have different trajectories (Panasenco *et al.*, 2011, 2012). Here, while both segments of the erupting prominence have different trajectories than the CME, both stay inside the expanding CME envelope.

The trajectory of the CME itself was determined by using T&T on the leading edge of the CME as discussed in Liewer *et al.* (2011). The reconstructions of the leading edge using both COR1 and COR2 stereoscopic pairs are shown in Figure 15. The COR1 data (first six reconstructions) span the time from 31 August 21:15:00 to 22:05:00 UT and the COR2 data (last 10 reconstructions) cover the time from 31 August 23:07:30 to September 1 03:37:30 UT. The 3D height-time plot for the CME from the reconstruction is shown in Figure 16. The direction of propagation determined from the reconstructions is Carrington longitude 210° and latitude −20°; the velocity is 312 km s^{-1}. Also shown for comparison is the latter portion of the height-time plot for the primary prominence segment (see Figure 6).

Figure 17 compares the latitude and longitude of various features of the eruption; it includes both trajectories and surface features. The thick solid line is the trajectory of the top of the primary filament segment determined by following the top of the 3D reconstructions shown in Figure 7. The solid diamond indicates the direction of propagation of the CME as determined from T&T; the open circle (O) indicates the approximate direction of propagation for the secondary filament (*cf.* Figures 13 and 14) for the time span 21:20 – 21:30 UT. Also shown are the surface locations of the U-shaped filament spine on 23 August (dash dotted line) and the flare ribbons on 31 August at 20:58:45 UT (dashed lines). From Figures 2 and 7 it can be seen that the pre-eruption filament spans a much large region in longitude and latitude than the flare ribbons; the flare ribbons presumably only become visible in stronger magnetic field regions. We also show the locations of the two EUV brightenings (X's), which Wang, Muglach, and Kliem (2009) found often lie near the outer edge of the transient coronal hole formed by the CME. Thus the X's probably mark the location of the CME legs.

Figure 17 shows the much larger deflection in latitude from the source region of the primary segment of the prominence compared to that of the CME. The CME, however, has a larger deflection in longitude. Non-radial effects on the CME are caused by the larger
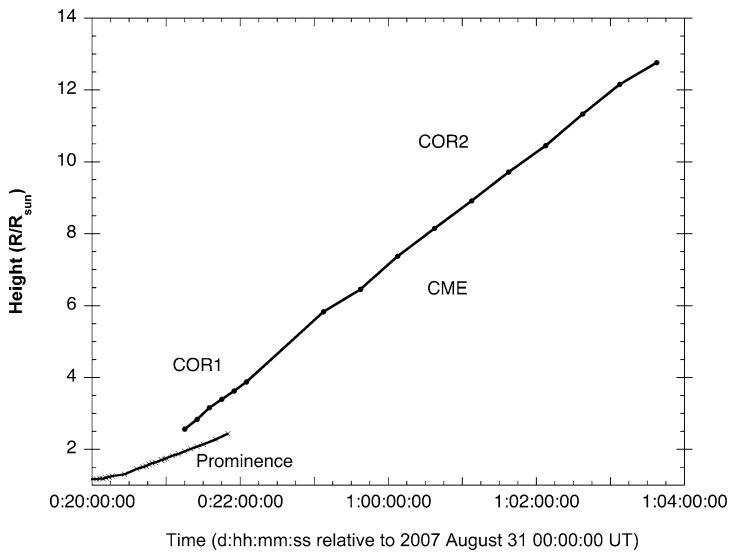
Figure 16 3D height-time plot for the CME from the reconstructions shown in Figure 16. Also shown is the height-time plot of the filament eruption starting from 31 August 2007 at 20 UT (Figure 6).

Figure 17 Trajectory of top of primary filament segment (thick solid line) using the reconstructions in Figure 7 and the directions of propagation of CME (solid diamond) and the secondary filament segment (O) shown in Figures 13 and 14. Also shown are the surface locations of the U-shaped prominence spine on 23 August (dash dotted line), the flare ribbons on 31 August at 20:58:45 UT (dashed lines) and of the observed EUV brightenings (X's).
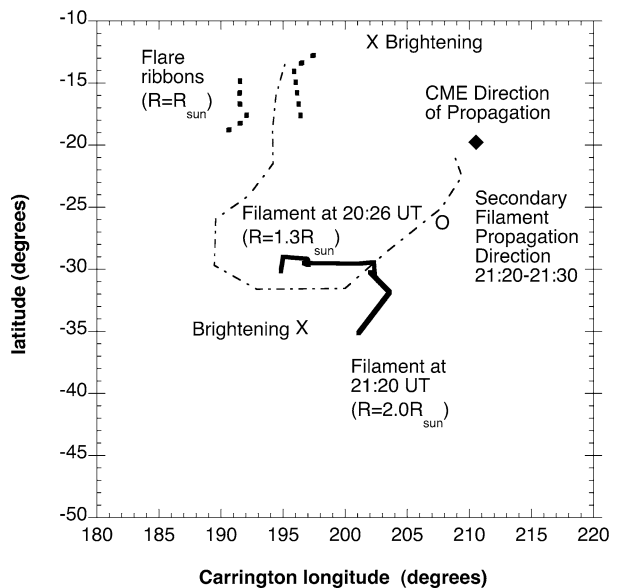
scale magnetic structure of the corona, while the non-radial motion of the filament is at first governed by asymmetries in the lower lying arcade fields (Panasenco *et al.*, 2011, 2012; Pevtsov, Panasenco, and Martin, 2012). Insight into the differences in the non-radial motion of the main prominence segment and the CME can be gained by examining the structure of the corona as computed from a potential-field source-surface (PFSS) model; here we use the model of Schrijver and De Rosa (2003).
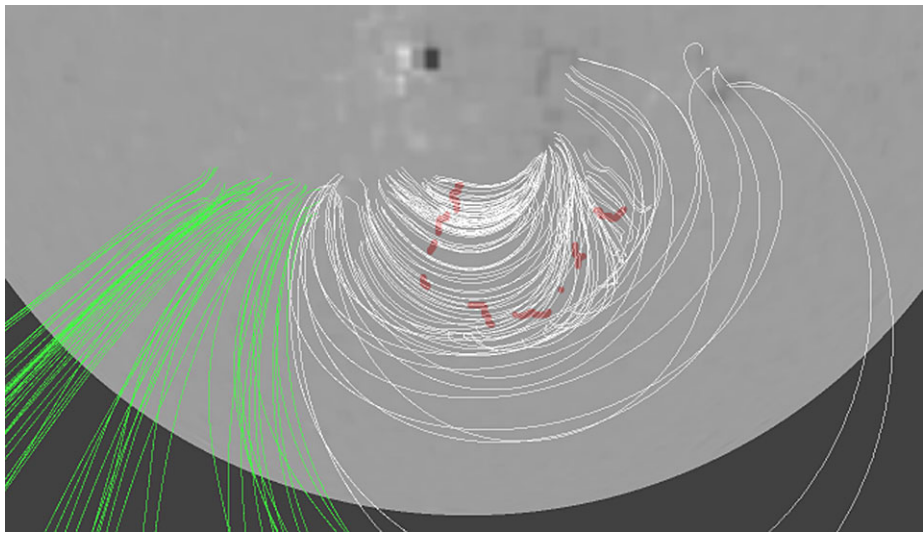
Figure 18 PFSS extrapolation of the coronal loops overlying the filament channel (white lines) and the open solar magnetic field of the coronal hole (green lines) on 27 August 2007 at 06:04 UT as viewed from Earth; the location of the Hα filament on the same day is shown in red. The higher surface density of arcade field lines on the east of the U indicates a stronger magnetic field.

The structure of the lower arcade fields overlying the filament channel is shown in Figure 18 (white lines); the open field lines of the neighboring coronal hole are also shown (green lines). The location of the filament on this day (at 06:01 UT), as seen in Hα, is shown in red (see also Figure 3, bottom panel). The asymmetry is apparent: the field is stronger on the side near the coronal hole (field line density is greater at the surface). This is the asymmetry responsible for the rolling motion and deflection of the prominence away from the coronal hole as discussed in Section 4.1 and shown in Figure 8. The CME, though deflected less than the main prominence strand in latitude from the source region, is deflected by about 20° in longitude by the coronal fields.

Figure 19 shows the magnetic field lines from the same PFSS model viewed from higher up in the corona. The CME trajectory is affected by the magnetic fields of the steamer that overlies the magnetic regions encompassing the entire U-shaped filament system and the decaying active region to the northwest. The CME is being guided in the general direction of the magnetic null line of the streamer, separating the green and magenta open magnetic field lines. The null line of the steamer is at approximately Carrington longitude 230° and latitude −45°. This can be compared with the approximate CME propagation direction shown in Figure 17 (longitude 210°, latitude −22°).

What is the cause of this filament/CME eruption? The filament retained its basic U shape as it crossed the disk. No particular activations or other activity seemed to affect the stability of the filament; it survived major eruptions nearby on 23 and 24 August. The most notable effect observed was the continual evolution of the magnetic fields in the surrounding region. Specifically, an analysis of the magnetograms showed that the negative polarity flux of the new active region to the NE of the U-shape spine spread into and canceled with the positive flux to the east of the filament leg which erupted. Over the course of the seven days leading up to the eruption, the positive radial magnetic flux of the overlying arcade field to the east of the U decreased by about a factor of 3 (from $\approx 4 \times 10^{20}$ Mx (maxwell) to
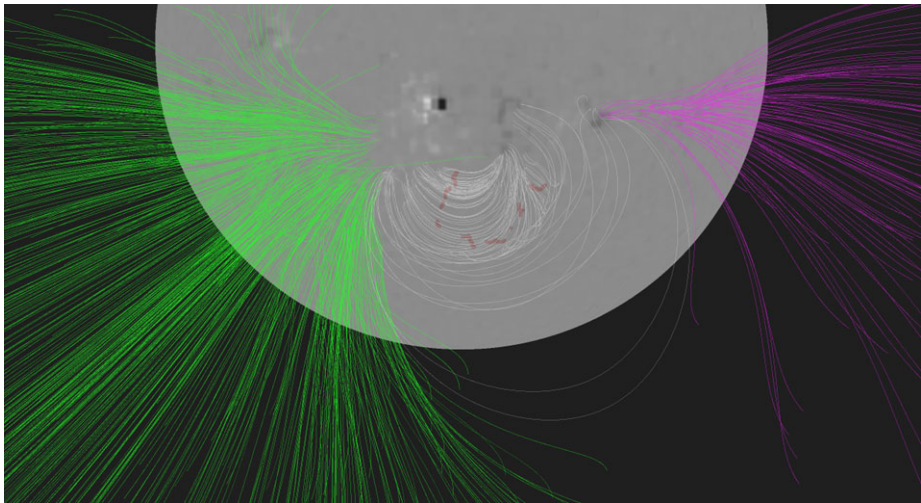
Figure 19 PFSS extrapolation of the open solar magnetic field of the coronal streamer (green and magenta lines) and the coronal loops overlying the filament channel (white lines) on 27 August 2007 at 06:04 UT as viewed from Earth; again, the location of the Hα filament is shown in red.

$\approx 1.5 \times 10^{20}$ Mx), with most of this decrease in the last two days. This would cause a weakening of the arcade fields over the left segment of the filament (a.k.a. "tether cutting"), which we interpret as leading to the observed slow rise (*cf.* Figure 6). At some point, consistent with the concept of Démoulin and Aulanier (2010), the filament must have reached the critical height at which the overlying arcade could no longer balance the upward magnetic stresses of the sheared magnetic field lines of the filament and cavity, leading to a loss of equilibrium (fast-rise phase) and the CME eruption.

6. Summary and Discussion

In this paper, the stereoscopic technique of tie-point and triangulation has been used to analyze the prominence and CME eruptions of 31 August 2007 using data from the STEREO spacecraft. This technique has allowed us to reconstruct in 3D many features associated with these eruptions in a heliocentric coordinate system. We were able to study the spatial relationships among various features of the eruption including the pre-eruptive prominence, flare ribbons, the erupting prominence, new filament endpoints formed during the eruption, the EUV brightenings, and the CME cavity. The stereoscopic analysis also allows us to compare trajectories of erupting filament strands and the CME and to establish the temporal relationship between the filament rotation and CME formation.

The U-shaped filament was stable for its entire passage across the solar disk until the eastern segment (only) erupted spectacularly as it reached the east limb. The western segment was still visible as it rotated over the west limb. We were able to reconstruct the prominence before and during the eruption using images in both extreme ultraviolet and white light. Prior to the eruption, we were able to reconstruct in 3D, for the first time, a filament barb connecting the spine to the solar surface. A barb is a bundle of field-aligned threads of a filament, which terminate in an opposite polarity inclusion within the dominant polarity region on one side of the filament channel, as described by Martin (1998). Using the bearing

of the barb (left relative to the spine) and the magnetogram, the filament was determined to be sinistral and the helicity of the system positive. From 3D reconstructions using data from both the EUVI instrument and COR1, we determined that the prominence rotates clockwise through about 90° as it erupts, as had been reported previously by Bemporad, Mierla, and Tripathi (2011). The rotation is in the direction expected for such a right-handed system and brings the expanding magnetic field lines of the prominence into closer alignment with the magnetic field of the overlying loop system.

A clear transition from slow to fast rise phase of the erupting filament is observed in the "true" (3D) height-time plot; while rotation begins in the slow rise phase, most of the rotation occurs in the fast rise phase, after CME formation has begun. As the filament erupts, the endpoints where it connects to the surface are observed to change and move away from the filament channel; Fan-shaped EUV brightenings are observed at the locations of the new endpoints. These observations are consistent with the analysis of filament eruptions and EUV brightenings reported by Wang, Muglach, and Kliem (2009). The new endpoints, which appear near the beginning of the fast-rise phase, are also sites of strong downflows. They are consistent with the interpretation by Wang, Muglach, and Kliem (2009) that the brightenings are the footpoints of current sheets formed where the prominence magnetic fields are reconnecting with the overlying arcade field during the eruption. Wang, Muglach, and Kliem (2009) also find that these brightenings mark the outer edge of transient coronal holes formed as the CME erupts and thus they may mark the outer edge of the CME legs.

Only with the stereoscopic viewpoints and analysis can we measure deflections in longitude as well as latitude from the source region. Here, both the CME and prominence showed considerable deflections in both. The filament described was typical in that it exhibited larger non-radial motions than its associated CME. The stereoscopic analysis also showed that the primary segment of the prominence exhibited the roll effect prior to CME formation, as observed in many non-radial prominence eruptions (Martin, 2003; Panasenco and Martin, 2008; Panasenco *et al.*, 2011, 2012). We attribute the prominence's gradual deviation from radial motion and its roll to asymmetry in the arcade overlying the filament in the low corona prior to CME formation. The CME, responding to magnetic fields higher up in the corona, gradually changes in trajectory in both longitude and latitude as it is guided towards the null line of the coronal streamer overlying the entire U-shaped filament channel and the neighboring active regions.

From the quite different directions of motion of the filament from the overlying coronal fields forming the CME, we infer that the filament, although constrained by the surrounding coronal field, had its own magnetic fields, separate from the overlying coronal field. We have shown here that the filament barb extends from the spine down to the solar surface, which is inconsistent with the concept of a pre-existing flux rope supporting and isolating the filament from the surface. Assuming the EUV brightenings mark the legs of the CME, we have also shown that the CME footpoints are at a different location than the original filament footpoints. These observations are consistent with the concept that the filament magnetic fields configuration is constrained by the surrounding coronal magnetic field, but not supported by the surrounding coronal loop system either before or during their eruption. The observations are also consistent with the concept of Démoulin and Aulanier (2010) that a CME results when the filament reaches a critical height at which the overlying arcade can no longer balance the upward magnetic stresses of the sheared magnetic field lines of the filament and cavity, leading to a loss of equilibrium (fast-rise phase) and the CME eruption.

References

Aschwanden, M.J., Wuelser, J.-P., Nitta, N., Lemen, J.: 2008, *Astrophys. J.* **680**, 1477.

Bemporad, A.: 2009, *Astrophys. J.* **701**, 298.

Bemporad, A., Mierla, M., Tripathi, D.: 2011, *Astron. Astrophys.* **531**, A147 (Correction: 2012 *Astron. Astrophys.* **531**, C1).

Démoulin, P., Aulanier, G.: 2010, *Astrophys. J.* **718**, 1388.

Gibson, S., Kucera, T.A., Rastawicki, D., Dove, J., de Toma, G., Hao, J., *et al.*: 2010, *Astrophys. J.* **724**, 1133.

Gopalswamy, N., Shimojo, M., Lu, W., Yashiro, S., Shibasaki, K., Howard, R.A.: 2003, *Astrophys. J.* **586**, 562.

Gosain, S., Schmieder, B., Venkatakrishnan, P., Chandra, R., Artzner, G.: 2009, *Solar Phys.* **259**, 13.

Howard, R.A., Moses, J.D., Vourlidas, A., Newmark, J.S., Socker, D.G., Plunkett, S.P., *et al.*: 2008, *Space Sci. Rev.* **136**, 67.

Inhester, B.: 2006, arXiv:astro-ph/0612649.

Kaiser, M.: 2005, *Adv. Space Res.* **36**, 1483.

Liewer, P.C., de Jong, E.M., Hall, J.R., Howard, R.A., Thompson, W.T., Culhane, J.L., Bone, L., van Driel-Gesztelyi, L.: 2009, *Solar Phys.* **256**, 57.

Liewer, P.C., Hall, J.R., Howard, R.A., de Jong, E.M., Thompson, W.T., Thernisien, A.: 2011, *J. Atmos. Solar-Terr. Phys.* **73**, 1173.

Li, T., Zhang, J., Zhao, H., Yang, S.: 2010, *Astrophys. J.* **720**, 144.

Li, T., Zhang, J., Zhao, H., Yang, S.: 2011, *Astrophys. J.* **739**, 43.

Martin, S.F.: 1998, *Solar Phys.* **182**, 107.

Martin, S.F.: 2003, *Adv. Space Res.* **32**, 1883.

Martin, S.F., Lin, Y., Engvold, O.: 2008, *Solar Phys.* **250**, 31.

Martin, S.F., Panasenco, O., Engvold, O., Lin, Y.: 2008, *Ann. Geophys.* **26**, 3061.

Mierla, M., Inhester, B., Antunes, A., Bousier, Y., Byrne, J.P., Colaninno, R., *et al.*: 2010, *Ann. Geophys.* **28**, 203.

Panasenco, O., Martin, S.: 2008, In: Howe, R., Komm, R.W., Balasubramaniam, K.S., Petrie, G.J.D. (eds.) *Subsurface and Atmospheric Influences on Solar Activity*, *ASP Conf. Ser.* **383**, 243.

Panasenco, O., Martin, S., Joshi, A.D., Srivastava, N.: 2011, *J. Atmos. Solar-Terr. Phys.* **73**, 1129.

Panasenco, O., Martin, S.F., Velli, M., Vourlidas, A.: 2012, *Solar Phys.* submitted.

Pevtsov, A.A., Panasenco, O., Martin, S.F.: 2012, *Solar Phys.* **277**, 185.

Schrijver, C.J., De Rosa, M.L.: 2003, *Solar Phys.* **212**, 165.

Thompson, W.T.: 2011, *J. Atmos. Solar-Terr. Phys.* **73**, 1138.

Wang, Y.-M., Muglach, K., Kliem, B.: 2009, *Astrophys. J.* **699**, 133.

Wuelser, J.-P., Lemen, J.R., Tarbell, T.D., Wolfson, C.J., Cannon, J.C., Carpenter, B.A., *et al.*: 2004, In: Fineschi, S., Gummin, M.A. (eds.) *Telescopes and Instrumentation for Solar Astrophysics*, *Proc. SPIE* **5171**, 111.

Xu, Y., Jing, J., Wang, H.: 2010, *Solar Phys.* **264**, 81.